

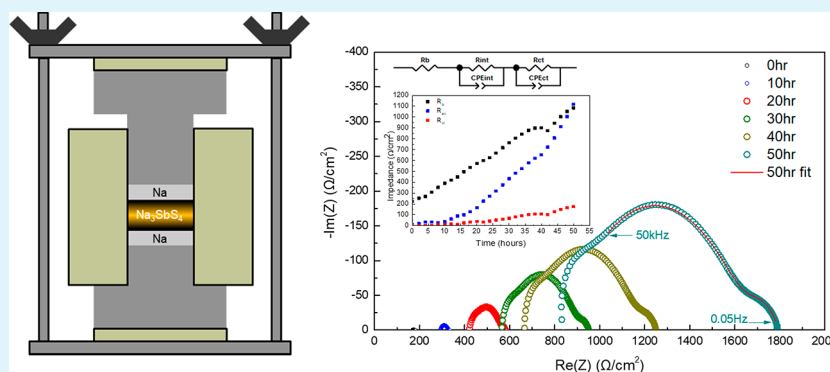
# New Insights into the Interphase between the Na Metal Anode and Sulfide Solid-State Electrolytes: A Joint Experimental and Computational Study

Erik A. Wu,<sup>†</sup> Christopher S. Kompella,<sup>†</sup> Zhuoying Zhu,<sup>†</sup> Jungwoo Z. Lee,<sup>†</sup> Steven C. Lee,<sup>†</sup> Iek-Heng Chu,<sup>†</sup> Han Nguyen,<sup>†</sup> Shyue Ping Ong,<sup>†,‡,§</sup> Abhik Banerjee,<sup>\*,†</sup> and Ying Shirley Meng<sup>\*,†,‡,§</sup>

<sup>†</sup>Department of NanoEngineering, University of California, San Diego, La Jolla, California 92093-0448, United States

<sup>‡</sup>Sustainable Power and Energy Center (SPEC), University of California, San Diego, 9500 Gilman Drive, La Jolla, California 92093-0448, United States

## Supporting Information



**ABSTRACT:** In this work, we investigated the interface between the sodium anode and the sulfide-based solid electrolytes  $\text{Na}_3\text{SbS}_4$  (NAS),  $\text{Na}_3\text{PS}_4$  (NPS), and Cl-doped NPS (NPSC) in all-solid-state-batteries (ASSBs). Even though these electrolytes have demonstrated high ionic conductivities in the range of  $1 \text{ mS cm}^{-1}$  at ambient temperatures, sulfide solid-state electrolytes (SSEs) are known to be unstable with Na metal, though the exact reaction mechanism and kinetics of the reaction remain unclear. We demonstrate that the primary cause of capacity fade and cell failure is a chemical reaction spurred on by electrochemical cycling that takes place at the interface between the Na anode and the SSEs. To investigate the properties of the Na-solid electrolyte interphase (SSEI) and its effect on cell performance, the SSEI was predicted computationally to be composed of  $\text{Na}_2\text{S}$  and  $\text{Na}_3\text{Sb}$  for NAS and identified experimentally via X-ray photoelectron spectroscopy (XPS). These two compounds give the SSEI mixed ionic- and electronic-conducting properties, which promotes continued SSEI growth, which increases the cell impedance at the expense of cell performance and cycle life. The SSEI for NPS was similarly found to be comprised of  $\text{Na}_2\text{S}$  and  $\text{Na}_3\text{P}$ , but XPS analysis of Cl-doped NPS (NPSC) showed the presence of an additional compound at the SSEI,  $\text{NaCl}$ , which was found to mitigate the decomposition of NPS. The methodologies presented in this work can be used to predict and optimize the electrochemical behavior of an all-solid-state cell. Such joint computational and experimental efforts can inform strategies for engineering a stable electrolyte and SSEI to avoid such reactions. Through this work, we call for more emphasis on SSE compatibility with both anodes and cathodes, essential for improving the electrochemical properties, longevity, and practicality of Na-based ASSBs.

**KEYWORDS:** solid-state electrolyte, sodium ion, ionic conductivity, anode interface, solid electrolyte interphase

## INTRODUCTION

Liquid electrolytes are the dominant technology used in lithium-ion (Li-ion) batteries as they have suitable properties such as high ionic conductivity, intimate contact with electrodes, and allow for the formation of a stable SEI that enables long-term battery cycling. However, liquid electrolytes typically contain toxic, flammable, and corrosive materials.<sup>1,2</sup> These hazards become more pronounced when pertaining to large-scale energy storage applications. To ameliorate this issue, solid-state electrolytes (SSEs) are gaining traction as they do

not contain such flammable components, thus avoiding the possibility of catastrophic failure. A practical SSE would make batteries lower maintenance and enable even longer cycling life. Furthermore, the use of metallic Li or Na as the anode, which would dramatically increase the energy density of the battery, is not achievable with current conventional liquid electrolyte cells.

**Received:** December 14, 2017

**Accepted:** March 12, 2018

**Published:** March 12, 2018

For these reasons, research interest in SSEs has been steadily growing.<sup>3</sup>

However, SSEs also have their drawbacks, such as having an ionic conductivity typically an order of magnitude lower than liquid electrolytes and inherently poorer contact with neighboring electrodes.<sup>4,5</sup> Much of the previous effort in SSE research was directed toward increasing the ionic conductivity to be comparable with liquid electrolytes with a now oft-stated benchmark value of at least 1 mS cm<sup>-1</sup> at room temperature.<sup>6</sup> The recent development of Li<sub>10</sub>GeP<sub>2</sub>S<sub>12</sub>, a solid electrolyte that has a reported room temperature conductivity of 12 mS cm<sup>-1</sup>, has driven further interest in SSEs as this number is comparable to or even exceeds that of commonly used liquid electrolytes.<sup>4</sup> Recently, many new SSEs with high ionic conductivities have been developed and reported.<sup>7</sup>

In parallel to the development of Li-ion-conducting SSEs is the rise in interest in Na-ion conductors for all-solid-state batteries. To that end, many Na analogues to Li-ion conducting SSEs have been explored both computationally and experimentally.<sup>8–10</sup> All-solid-state Na-ion batteries have the potential to be a lower-cost alternative; Na is orders of magnitude more abundant than Li in the Earth's crust, which makes the cost of Na around 20–30 times less than Li.<sup>5,8</sup> The precursors to synthesize Na-ion conducting solid electrolytes are readily available Na salts or compounds. Furthermore, the electrochemical behavior of Na is similar to that of Li. Although Na has a redox potential of -2.70 V compared to -3.04 V for Li (versus standard hydrogen electrode), the significant cost reduction for raw Na metal suggests that Na batteries can still occupy a market space where cost is a more important consideration than having the absolute highest energy density.<sup>5,8</sup> One such application is the aforementioned large- or grid-scale energy storage.<sup>11,12</sup>

An ideal Na solid-state electrolyte must have several properties, among which are an ionic conductivity of 1 mS cm<sup>-1</sup> or greater at room temperature, intimate contact with solid electrodes, the ability to operate over a wide electrochemical window, and have good stability against elemental Na.<sup>3</sup> However, no single electrolyte material or class of materials currently possesses every one of these characteristics.<sup>13</sup> As an example, much research effort has been put into SSEs such as  $\beta$ -alumina and NASICON, but these oxides exhibit good conductivity only at elevated temperatures.<sup>14–18</sup>

Chalcogenides, or S- and Se-based compounds, have been shown to have favorable properties for use as a solid-state electrolyte.<sup>16</sup> Although they have their own issues such as air and moisture sensitivity, they have potentially higher ionic conductivities<sup>15,19–21</sup> and a lower Young's modulus compared to those of oxide materials.<sup>19,22</sup> A more elastic solid electrolyte would be more able to accommodate volume changes associated with the intercalation and deintercalation of Li<sup>+</sup> or Na<sup>+</sup> ions without the onset of cracks or mechanical failure. Another benefit of sulfides is that they do not need energy-intensive processing steps such as high-temperature sintering to obtain a high ionic conductivity value; oxides usually require this to overcome a larger grain boundary impedance, but for chalcogenides, room-temperature cold-pressing is sufficient.<sup>23,24</sup> Various Na solid electrolytes have been studied, among them Na<sub>3</sub>PS<sub>4</sub> and Na<sub>3</sub>PSe<sub>4</sub>.<sup>10,21,25–29</sup> It was postulated that selenides have conductivity greater than that of sulfides as a larger unit cell would subsequently have more channels for Na-ion conduction. For example, Na<sub>3</sub>PSe<sub>4</sub> has a room temperature conductivity of 1.16 mS cm<sup>-1</sup> compared to 0.2 mS cm<sup>-1</sup> for

Na<sub>3</sub>PS<sub>4</sub>. Because the SbS<sub>4</sub><sup>3-</sup> ion is similar in size to the PSe<sub>4</sub><sup>3-</sup> ion, NAS could also have a favorable structure to be used as an SSE, and indeed, NAS has been reported to have an ionic conductivity in the range of 1 mS cm<sup>-1</sup>.<sup>23,24</sup> Along with structural modification, aliovalent doping has also been proven to increase ionic conductivities on sulfide-based glasses and glass-ceramics.<sup>21,24,30–33</sup> Our previous work highlighted Cl-doped tetragonal Na<sub>3</sub>PS<sub>4</sub> (NPSC), which demonstrated an ionic conductivity exceeding 1 mS cm<sup>-1</sup>.<sup>25</sup>

Although several sulfide SSEs have demonstrated high ionic conductivity, they also have the persistent problem of instability when put in contact with Na metal.<sup>23,34</sup> In this work, phase pure NAS, NPS, and NPSC were all successfully synthesized, their electrochemical properties were evaluated, and the species at the SSEI were investigated via computation, electrochemical experiments, and material characterization techniques. The aim in this investigation is to highlight degradation mechanisms such as unwanted reactions between the electrolyte and electrodes in an ASSB. We emphasize that although ionic conductivity of an electrolyte is important, elucidating the failure mechanisms of all-solid-state full cells can provide critical insights for further screening of SSEs, subsequent evaluation of compatible ASSB chemistries, and engineering of their electrochemical interfaces.

## METHODS

Due to the sensitivity of the precursor compounds and the SSEs to water and air, all synthesis and electrochemical testing steps took place in an Ar-filled glovebox (MBraun MB 200B, H<sub>2</sub>O < 0.5 ppm, O<sub>2</sub> < 1.0 ppm) unless otherwise specified.

**Synthesis of NAS, NPS, and NPSC.** Solid-state synthesis of NAS was achieved by mixing Na<sub>2</sub>S (99%, Sigma-Aldrich), Sb powder (99.999%, Alfa Aesar), and S (99.998%, Sigma-Aldrich) in a mortar and pestle for 30 min in the ratio outlined by eq 1.



The mixture was pressed into a 13 mm diameter pellet (Carver) at 370 MPa, broken up into small pieces, loaded into a quartz tube, and capped with a rubber septum. The edges of the septum were wrapped with paraffin film (Parafilm "M"). The tube was brought outside of the glovebox, connected to vacuum, flame-sealed, and heat-treated in a box furnace. The temperature was ramped to 550 °C over 1.5 hours, kept at 550 °C for 24 h, and subsequently naturally cooled to room temperature. The quartz tube was brought back into the glovebox where the material was extracted and placed into a ball mill jar with 11 10 mm diameter ZrO<sub>2</sub> grinding balls. The jar was sealed tightly in the glovebox to prevent ambient oxygen and water to be introduced upon removal of the jar from the glovebox. The material was ball-milled at 370 rpm over a duration of 20 h with 15 min grinding and 15 min rest intervals using a Retsch PM 100 Planetary Ball Mill. The jar was brought back into the glovebox, and the material was extracted for further testing.

Pure tetragonal Na<sub>3</sub>PS<sub>4</sub> (t-Na<sub>3</sub>PS<sub>4</sub>) was synthesized via solid-state reaction following the methods outlined in a previous work.<sup>25</sup> The material was synthesized from Na<sub>2</sub>S (99%, Sigma-Aldrich) and P<sub>2</sub>S<sub>5</sub> (99%, Sigma-Aldrich). The precursors were ground with an agate mortar and pestle in a molar ratio of 75:25, respectively. To introduce the chloride dopant, NaCl (99.99%, Alfa Aesar) was mixed into the previous precursors according to eq 2:



The resulting mixture was then flame-sealed under vacuum in a quartz tube and heat-treated in a box furnace. The temperature was ramped to 850 °C over 6 h and then immediately quenched in water containing dry ice. Subsequently, the sample was reintroduced into the

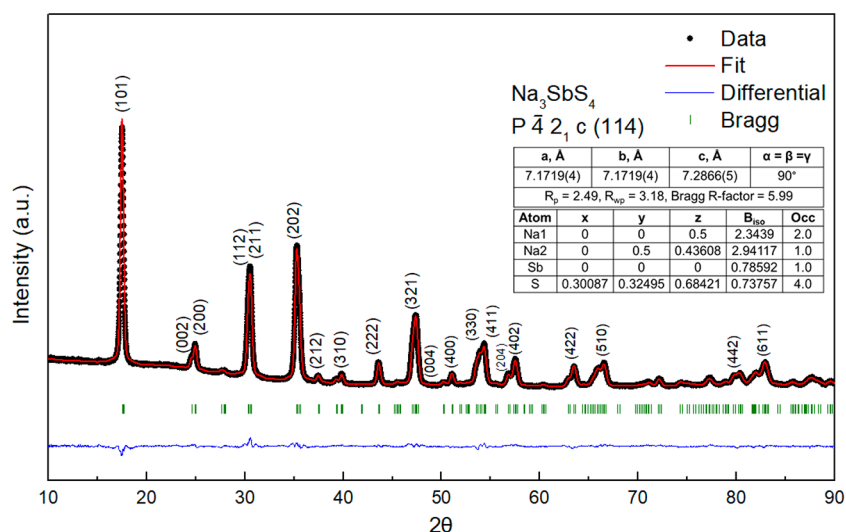


**Figure 1.** XRD data of heat-treated, postball-milled NAS. Inset: Rietveld refinement results, detailing lattice parameters, R-factors, atomic positions, thermal factors, and atom occupancies.

glovebox, ground in a mortar and pestle, flame-sealed, and heat-treated again at 420 °C for 3 h to stabilize the tetragonal phase.

**X-ray Diffraction: NAS.** A 0.5 mm-diameter boron-rich capillary glass tube (Charles Supper) was loaded with a few milligrams of the  $\text{Na}_3\text{SbS}_4$  powder after ball-milling. The tube opening was capped with clay and wrapped in paraffin film before being brought outside of the glovebox, where it was flame-sealed using a hand-held butane torch.

The sample was fixed in the Bragg–Brentano  $\theta$ – $\theta$  configuration, and the Debye–Scherrer method was used. The samples were measured on a Bruker Kappa goniometer equipped with a Bruker Vantec 500 detector. XRD data was collected using Cu  $K\alpha$  radiation at 45 kV and 50 mA, over a  $2\theta$  range of 5–90° with a step size of 0.01°. Rietveld refinement was conducted using the FullProf software suite.<sup>35</sup>

**Electrochemical Impedance Spectroscopy (EIS): NAS.** The ball-milled NAS powder was pressed into a 13 mm polyether ether ketone (PEEK) die using two titanium plungers at a pressure of 370 MPa. The thickness of the pellet was recorded. Carbon powder was applied to both sides of the die to serve as blocking electrodes and to improve contact with the titanium current collectors. The carbon was pressed onto the NAS pellet at 370 MPa. The test cell was then secured into a cell holder and connected to a Solartron 1260 impedance analyzer. Impedance measurements were taken with an applied AC potential of 50 mV over a frequency range of 1 MHz to 1 Hz. The Nyquist plot was fit to an equivalent circuit model similar to a Randles circuit with the exception of using constant phase elements (CPEs) instead of capacitors to account for any nonideal capacitive behavior such as a nonuniform electrode surface.<sup>36</sup> Temperature-dependent impedance measurements were collected by heating the cell inside a box furnace inside the glovebox. The temperature was raised from 25 to 95 °C in 10 °C increments. For every increment, the heating rate was 1 °C  $\text{min}^{-1}$ , and the target temperature was held for an hour to allow for the temperature to stabilize before the EIS measurement was taken. The activation energy ( $E_a$ ) for Na ion diffusion was calculated from the slope of the resulting Arrhenius plot.

**Construction of Symmetric Cells for NAS, NPS, and NPSC.** For the symmetric cell construction, 250 mg of the ball-milled NAS powder was pressed into a 13 mm polyether ether ketone (PEEK) die using two titanium plungers at a pressure of 370 MPa. Na metal was pressed onto both titanium plungers to form a thin disc on the plunger surfaces. Excess Na metal and any visible surface oxidation was scraped away from the plunger. The plungers were placed into the PEEK die and pressed at 37 MPa. The pressure was released immediately, and the cell was subsequently fastened into the holder. EIS was measured every 2 h for a duration of 50 h using a frequency range of 1 MHz to 0.01 Hz and an applied potential of 50 mV.

For the NPS and NPSC symmetric cells, the same procedure was applied to construct the symmetric cells. Once constructed, a 50  $\mu\text{A}$  galvanic square-wave waves applied for 10 min, and then a reverse current was applied for the same duration to strip and plate Na metal, respectively. The voltage of the symmetric cell was measured, and the area-specific resistance (ASR) was calculated by Ohm's law.

**Construction of Full Cells for NAS, NPS, and NPSC.** The procedure to construct electrochemical full cells was the same regardless of the SSE used. Electrochemical cells were constructed using a Na metallic anode, solid electrolyte, and a composite cathode, consisting of the electrolyte mixed with ball-milled  $\text{TiS}_2$  in a 1:2 ratio. The composite cathode was newly mixed each time before making a cell. Two-hundred and fifty milligrams of the SSE powder was pressed at 370 MPa for 5 min in a 13 mm PEEK die. Roughly 10 mg of the composite cathode was measured, recorded, and placed onto the electrolyte on the tall titanium plunger side. The cathode was pressed at 370 MPa for 5 min to ensure complete coverage. Na metal was pressed onto the opposite side or the small titanium plunger in a similar manner as described for the symmetric cell. After pressing at 37 MPa, the cell was fastened into a holder.

All cells were galvanostatically cycled from 1.2 to 2.4 V using a Digatron cyler at a rate of C/10. Cycling was conducted at room temperature within the MBraun Ar-filled glovebox.

**In Situ Impedance: NAS.** A cell containing Na, 250 mg of NAS, and 10 mg of the  $\text{TiS}_2$ :NAS composite cathode was constructed as previously described. The cell was connected to the Solartron 1260 Impedance Analyzer and held at rest (open circuit voltage measurement) for 30 min. The cell was galvanostatically cycled from 1.2 to 2.4 V at a rate of C/5 for 5 cycles. Every time the cell reached 1.2 or 2.4 V, an EIS measurement was taken using a frequency range of 2 MHz to 0.01 Hz and an applied potential of 50 mV.

**Cyclic Voltammetry (CV): NAS.** An electrochemical cell was constructed as previously described, except instead of a NAS: $\text{TiS}_2$  composite cathode, a NAS:carbon 1:1 mixture (weight ratio) was used. The cell was connected to the Solartron 1260 impedance analyzer, where CV was conducted for 20 cycles between 1.2 to 2.4 V at a scan rate of 5  $\text{mV sec}^{-1}$ .

**Electrochemical Stability Analysis: NAS.** The electrochemical stability of NAS in contact with the electrodes is estimated using the Na grand potential approach, as detailed in our recent work.<sup>20</sup> In this approach, the solid electrolyte–electrode interface is modeled as an open system with respect to Na, and the relevant thermodynamic potential is the grand potential, given as  $\Phi \approx E - \mu_{\text{Na}} N_{\text{Na}}$ .  $E$ ,  $N_{\text{Na}}$ , and  $\mu_{\text{Na}}$  are total energy from density functional theory calculations and the number of Na atoms in the open system and Na chemical potential, respectively. Note that the chemical potential of Na is related to the

voltage vs Na/Na<sup>+</sup> (V) via the following relation, with  $V = -(\mu_{\text{Na}} - \mu_{\text{Na0}})$ , where  $\mu_{\text{Na0}}$  is the reference chemical potential of bulk Na metal. We evaluate the electrochemical stability of NAS against electrodes by constructing the Na–Sb–S ternary phase diagrams with Na chemical potential varying between  $\mu_{\text{Na0}}$  and  $(\mu_{\text{Na0}} - 3.5)$  eV.

The electronic conductivity of the phase equilibria at NAS/Na interface is also assessed by computing their electronic band gap. Given the well-known band gap underestimation by semilocal functionals,<sup>37</sup> the Heyd–Scuseria Ernzerhof (HSE)<sup>38,39</sup> hybrid functional is adopted. Nonspin-polarized calculations with a k-point density of 500/(number of atoms in the unit cell) were utilized.

**X-ray Photoelectron Spectroscopy (XPS).** The electrochemical cells were disassembled within the glovebox. To obtain the interphase samples, the Na metal was scraped off the small titanium plunger with a razor blade, and the powder of interest was then collected. For the standards, Na<sub>2</sub>S powder was collected as-is. Na<sub>3</sub>Sb was synthesized via a stoichiometric mixture of Na and Sb via ball milling for 2 h at 550 rpm, verified via XRD. Pristine Na<sub>3</sub>SbS<sub>4</sub> powder was directly collected after synthesis. All samples were placed into glass vials, and the vial caps were sealed with paraffin film.

The sealed vials were placed into a metal canister, and the metal lid was screwed tightly to prevent moisture and oxygen ingress during transport outside of the glovebox. The sealed metal canister was reintroduced into a glovebox, and the samples were mounted and transferred into the attached XPS tool (Kratos Axis Supra) from within the glovebox to avoid any exposure to ambient air. All measurements were taken using 15 kV Al K $\alpha$  radiation (with a 500 mm Rowland circle monochromator) at a chamber pressure of approximately 10<sup>-8</sup> Torr. For the survey scans, a pass energy of 160 eV and a dwell time of 100 ms was used. For the specific element region scans, a pass energy of 20 eV and a dwell time of 300 ms was used. For insulating samples such as Na<sub>2</sub>S, the charge neutralizer was enabled.

Data calibration, analysis, and fitting were all performed by using CasaXPS. All region spectra for a given compound were calibrated to their corresponding adventitious carbon peak (C 1s, 284.8 eV), and the spectra were fitted using a Shirley-type background.

## RESULTS AND DISCUSSION

**Synthesis and Ionic Conductivity of NAS.** To verify that phase-pure NAS was synthesized, XRD was conducted on the postball-milled Na<sub>3</sub>SbS<sub>4</sub> powder. The data and Rietveld refinement results are shown in Figure 1. The lattice parameters are consistent with the tetragonal phase of Na<sub>3</sub>SbS<sub>4</sub> and are in good agreement with previously published values; the structure was solved with the *P42<sub>1</sub>c* space group (no. 114). Thus, using Na<sub>2</sub>S and elemental Sb and S, phase pure NAS was synthesized. Ball-milling was conducted due to Zhang et al.'s statement that hand mixing results in a nonuniform particle size distribution unfavorable for cold-pressing.<sup>23</sup> The Rietveld refinement results show that NAS retains the tetragonal phase even after ball milling.

To measure the ionic conductivity, EIS of an NAS pellet with blocking electrodes was measured. The EIS data and Arrhenius plot can be seen in Figure 2. After fitting the Nyquist plot and normalizing for the pellet dimensions, the room temperature conductivity was determined to be 1.06 mS cm<sup>-1</sup>. The activation energy was calculated from the slope of the resulting Arrhenius plot and is 216 meV. These values are comparable to literature values; the ball-milled NAS has high room temperature ionic conductivity, as expected.<sup>21</sup>

**Full Cell Electrochemical Behavior: NAS.** Even though NAS possesses high Na ionic conductivity, to our knowledge, there have been no reports on cycling of a full cell that utilizes NAS and a Na metal anode. To evaluate the performance of NAS in a full cell configuration, cells were constructed with a Na anode, NAS SSE, and a composite cathode (TiS<sub>2</sub>:NAS in a

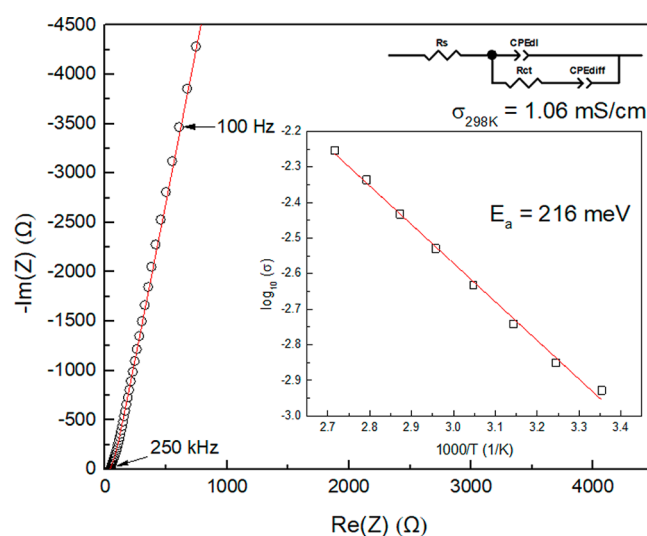


**Figure 2.** Room temperature Nyquist plot for ball-milled Na<sub>3</sub>SbS<sub>4</sub> with the corresponding equivalent circuit model. Inset: Arrhenius plot of Na<sub>3</sub>SbS<sub>4</sub> with the activation energy calculated from the slope.

1:2 ratio). The choice of the TiS<sub>2</sub> cathode is motivated by its suitable operating voltage ( $\sim 1.7$  V versus Na/Na<sup>+</sup>), its fast kinetics for Na<sup>+</sup> intercalation, as well as its high electronic conductivity.<sup>40,41</sup> The cell was galvanostatically cycled from 1.2 to 2.4 V with a current density of approximately 50  $\mu\text{A cm}^{-2}$ , corresponding to a C/10 rate. The typical cycling behavior of these cells is illustrated in Figure 3. The theoretical capacity of the NaTiS<sub>2</sub> active material is 198 mAh g<sup>-1</sup>. The initial charge capacity is 115.9 mAh g<sup>-1</sup>, yielding an initial Coulombic efficiency of 70.1%. One of the reasons that the observed specific capacity is lower than the theoretical is the low utilization of the cathode active material since the cathode composite was prepared via conventional hand mixing.

Rapid capacity fading is observed in the voltage profiles for the Na|NAS|NAS:TiS<sub>2</sub> full cell in Figure 3. The full cell lost over 92% of its capacity after 29 cycles which implies very poor cyclic stability. It is also interesting to note that around 98% of the capacity is retained between cycles 2–10, but eventually capacity fade becomes severe, until the cell can no longer cycle. This is certainly correlated with the polarization changes during cycling; there are negligible polarization changes for the first 10 cycles, but polarization becomes more pronounced upon subsequent cycling. Although NAS has a high ionic conductivity, the cyclic performance indicates that NAS is unstable against a Na metal anode. Capacity fade has also been observed in a Na<sub>15</sub>Sn<sub>4</sub>|NAS|NaCrO<sub>2</sub> full cell; therefore, it is crucial to understand the capacity fading mechanism for NAS.<sup>42</sup>

To explore the reason behind the increasing polarization and the capacity fade, CV was conducted on a Na|NAS|NAS:C (1:1 weight ratio) cell at a scan rate of 5 mV sec<sup>-1</sup> to evaluate the electrochemical stability of NAS within the operating voltage window of the TiS<sub>2</sub>-containing cell (1.2–2.4 V). It is worth mentioning that we use NAS-C ball milled composite as a cathode to run the CV for electrochemical stability test; similar methods to measure the electrochemical stability of LGPS and NPS have also been previously reported.<sup>43,44</sup> The cyclic voltammogram for NAS is shown in Figure S1 of the Supporting Information. The first cycle showed oxidation of NAS at a relatively low voltage of 1.4 V along with a larger anodic current as the voltage increased past 1.95 V, which

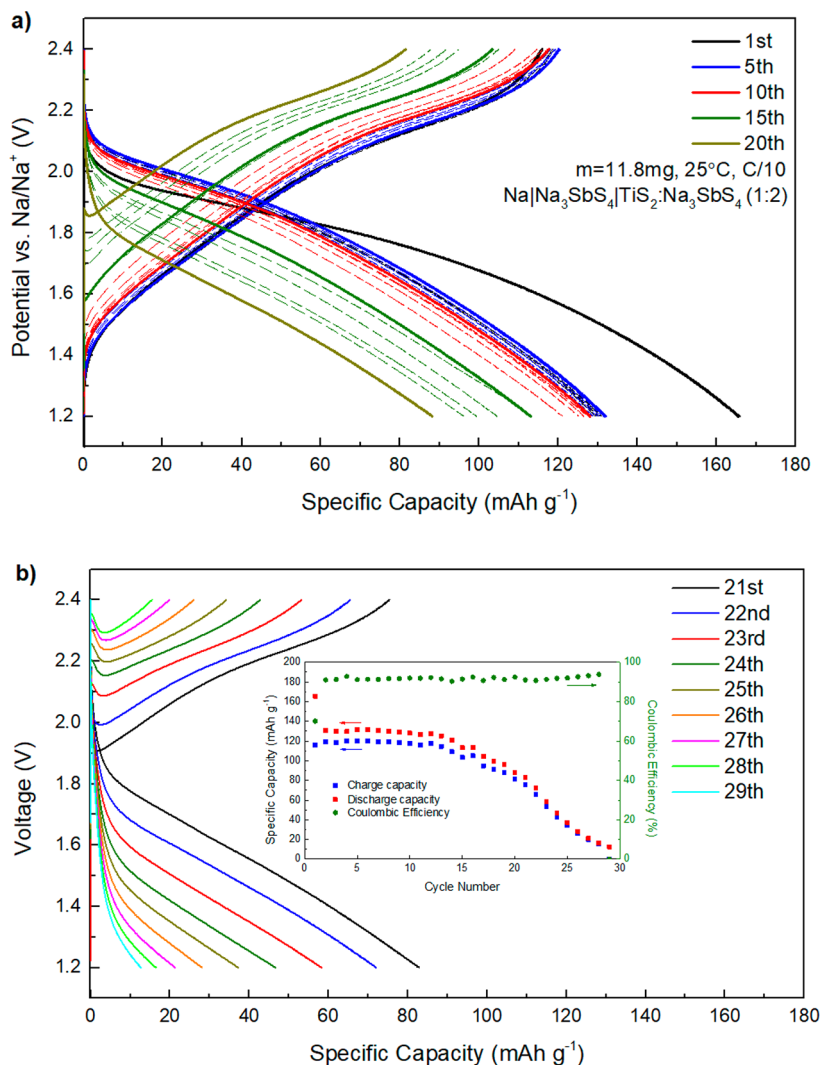


**Figure 3.** Electrochemical behavior of the Na|NAS|TiS<sub>2</sub>:NAS cell. (a) Voltage versus specific capacity for the first 20 cycles. Solid lines denote every fifth cycle, and the dotted lines are the intermediate cycles. (b) Cycles 21–29 for the same cell. Inset: Charge capacity, discharge capacity, and Coulombic efficiency versus cycle number.

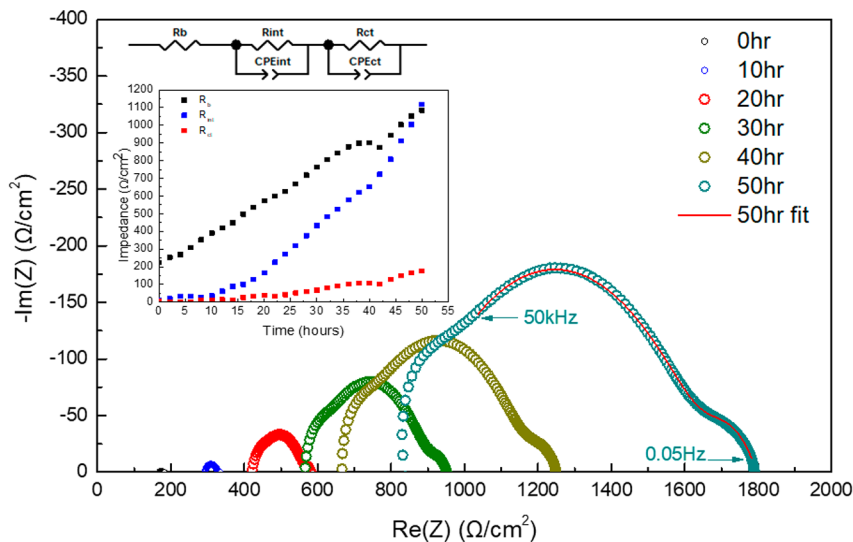


**Figure 4.** Nyquist plot of the Na|Na<sub>3</sub>SbS<sub>4</sub>|Na symmetric cell from 0 to 50 h, showing the increasing impedance with time. Inset: equivalent circuit used to fit the data with a corresponding fit plotted on the 50 h curve. Inset: the fitted impedance components with time.

corresponds with the reduction peak at 1.84 V. However, upon subsequent cycles, the anodic current decreases, and the current response for cycles 2–20 is close to identical. This is indicative of the formation of the SSEI during the first cycle, as the observed current does not steadily increase with continued cycling, instead showing reversible oxidation and reduction as cycling proceeds. Therefore, we believe that the electrochemical stability of NAS within the 1.2–2.4 V range does not contribute significantly to the observed poor cyclic performance of the full cell. Interestingly, LGPS was shown to have a narrow electrochemical stability window, but a full cell containing LGPS was still able to last for over 100 cycles.<sup>45</sup> The same observation was found in  $\text{Li}_3\text{PS}_4$ , which exhibited reversible oxidation and reduction within the voltage range of 0.8–3 V, and a cell lasted 300 cycles without a significant capacity loss.<sup>46</sup> This further suggests that degradation of NAS specifically within the 1.2–2.4 V voltage window is not the primary cause of the capacity fade and cell failure.

Because electrochemical instability is not the major issue, the chemical stability of NAS with  $\text{TiS}_2$  and Na metal was thus investigated. It is known that oxide cathodes react with sulfide SSEs, which results in severe capacity fading and low power performance. However, because NAS and  $\text{TiS}_2$  are sulfides, the chemical potential difference is comparatively negligible, and no chemical reaction at the NAS/ $\text{TiS}_2$  interface is expected. XRD spectra of  $\text{TiS}_2$  and NAS mixture was measured, and the results are shown in Figure S2. In the pristine sample, the main observable peaks are attributed to NAS, while after the first discharge and first charge, the onset of peaks from Na-intercalated  $\text{NaTiS}_2$  and  $\text{Na}_{0.55}\text{TiS}_2$  can be observed. The presence of these species in the charged sample can explain the initial irreversible capacity because that means not all the Na ions are extracted from  $\text{TiS}_2$ . More importantly, peaks from chemical reactions or from new phases are not present, clearly signifying chemical compatibility between NAS and  $\text{TiS}_2$ . While some Na ions remain in the  $\text{TiS}_2$  upon charging, this is not the main reason for the onset of the severe capacity fade in the full cell.

The anode or Na|NAS interface was studied by constructing a Na|NAS|Na symmetric cell. The cell sat at rest, and an EIS was recorded every hour over a time span of 50 h, and the Nyquist plot is shown in Figure 4. The cell was fit to an equivalent circuit to deconvolute the impedance contributions: the electrolyte resistance  $R_b$ , the SSEI resistance  $R_{\text{int}}$ , and the charge transfer resistance  $R_{\text{ct}}$  between the electrode and electrolyte.<sup>47</sup> Figure 4 shows that the magnitude of all of the components continually and gradually increases with time simply due to contact between NAS and Na metal without any biasing. We observe an increase in the bulk and charge transfer resistances, attributed to changes in the SSE as Na ions are continuously consumed from NAS to form and grow the SSEI. It is also interesting to notice that  $R_{\text{ct}}$  also increases for the symmetric cell, which could be increasing due to poorer contact of the Na with NAS arising from the growth of the SSEI.<sup>48</sup> Because the cathodic contribution on cell fading is negligible, this result indicates that the anodic contribution is the dominant factor.

As previously shown in Figure 3, the cell polarization increases as cycling proceeds, signifying a steady increase in the impedance of the cell as time goes on. This impedance increase over time is further suggested by the symmetric cell impedance in Figure 4. To correlate the symmetric cell impedance growth to the full cell behavior, impedance measurements of the full

cell after charging and discharging was also conducted, and the results are shown in Figure 5. The cell components were fit to

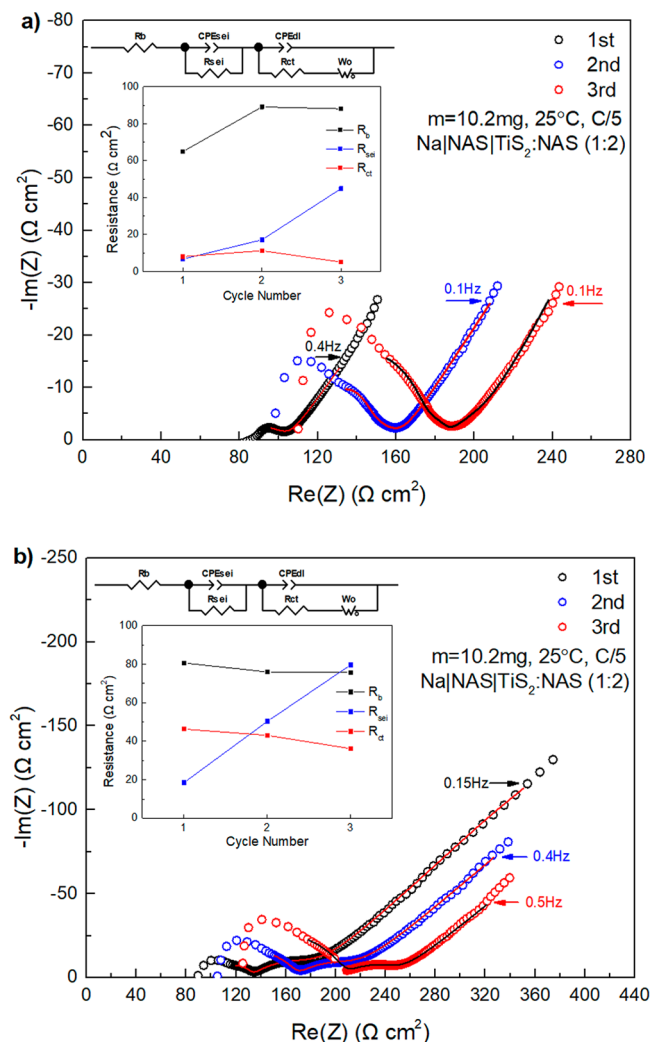


**Figure 5.** Full cell in situ impedance measurements for (a) first through third discharge and (b) first through third charge. Insets: fitted resistance components versus cycle number.

the Li-ion battery equivalent circuit model.<sup>49,50</sup> As cycling proceeds,  $R_{\text{sei}}$  is the only component with a significant increase, consistent with the symmetric cell results. It is important to note that  $R_{\text{sei}}$  increases more drastically upon subsequent charging, as seen in Figure 5b. This is intuitive because Na nucleates on the anode side during charging, which would expose it to NAS. This means the reaction with NAS is electrochemically facilitated during cycling. From both the symmetric cell and full cell impedance measurements, the Na|NAS interphase appears to be not static, but rather dynamic, or growing significantly with time. Previous reports indicated that LGPS formed a dynamic interface with Li metal due to the formation of ion-conducting ( $\text{Li}_3\text{P}$ ) and electronic-conducting components (Li–Ge alloy) at the interface.<sup>51</sup> In contrast, LPSI forms a stable SEI with Li metal as the SEI was a mixture of ionic-conducting and electronically insulating components, which prevents continued decomposition of the SSE.<sup>51</sup> The nature of the impedance at the Na|NAS interface clearly indicates that there must be an electronically conductive component at the SEI. So far there have been no studies on the

Na/NAS interface; therefore, it is necessary to find out the chemical species of the SSEI to explain their effects on the cycling behavior.

To predict the compounds at the Na/NAS interface, computation of the phase equilibria at the Na/NAS interface was conducted. Figure 6 shows the Na grand potential phase

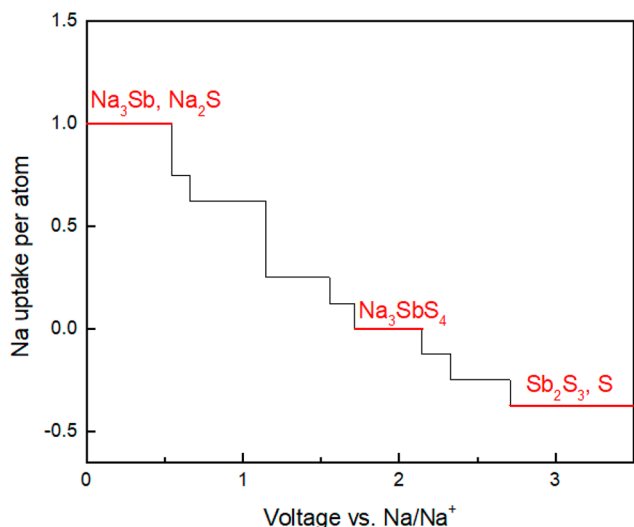


**Figure 6.** Na grand potential phase stability plots for  $\text{Na}_3\text{SbS}_4$ . In the anodic or low voltage region,  $\text{Na}_3\text{SbS}_4$  undergoes a reduction process and uptakes Na, whereas in the cathodic or high voltage region, it undergoes oxidation and loses Na. Compounds listed the plot are predicted phase equilibria at corresponding regions.

stability plot of the NAS solid electrolyte as a function of Na chemical potential. We find that at the Na/NAS interface, NAS decomposes into  $\text{Na}_3\text{Sb}$  and  $\text{Na}_2\text{S}$ , a known metallic alloy and an insulator at room temperature, respectively.<sup>52,53</sup> To confirm this, the electronic band gaps were calculated to be 0.68 and 3.22 eV for  $\text{Na}_3\text{Sb}$  and  $\text{Na}_2\text{S}$ , respectively (see Figure S3 of the Supporting Information). To experimentally investigate the compositions of the Na/NAS interface, XPS was conducted on the pristine electrolyte, the Na/NAS interface from a cycled cell, and the Na/NAS interface from a symmetric cell. Figure 7a

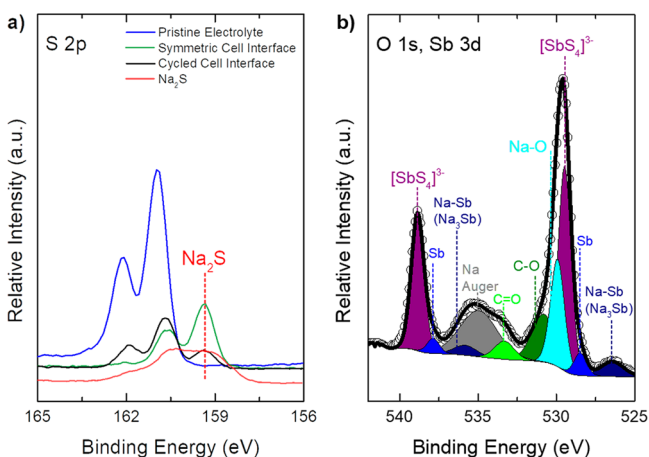


**Figure 7.** (a) S 2p region scan of the pristine NAS, anode interface of the cell cycled to completion, the symmetric cell, and the  $\text{Na}_2\text{S}$  precursor, overlaid on top of each other. (b) O 1s/Sb 3d region scan of the Na/NAS SSEI from the cell cycled to completion.

shows the S 2p region scan for these samples plus the scan for the  $\text{Na}_2\text{S}$  precursor. An example fit of the S region scan for the cycled anode interface sample shown in Figure S4. In addition, the peak positions and parameters for every component in our XPS fittings are detailed in Tables S1 and S2 of the Supporting Information. Compared to the pristine electrolyte, all samples that contacted Na have an additional peak at 159.4 eV, consistent with the binding energy of  $\text{Na}_2\text{S}$ ,<sup>54</sup> thus confirming  $\text{Na}_2\text{S}$  as a decomposition product at the Na/NAS interface.

As for  $\text{Na}_3\text{Sb}$ , there were no reports containing an XRD or XPS measurement for this compound to the best of our knowledge. Before the Sb 3d region of the SSEI could be analyzed,  $\text{Na}_3\text{Sb}$  had to be synthesized to serve as a measurement standard. The XRD pattern and the O 1s/Sb 3d XPS region scan of the as-synthesized  $\text{Na}_3\text{Sb}$  is shown in Figure S5 of the Supporting Information; phase-pure  $\text{Na}_3\text{Sb}$  was confirmed from the XRD measurement. In addition, the O 1s/Sb 3d XPS region scan of pristine NAS is shown in Figure S6. With these spectra, the O 1s/Sb 3d spectrum of the cycled anode–electrolyte interface, shown in Figure 7b, can be deconvoluted. Sb XPS peaks have a characteristic separation of 9.39 eV of the 3d orbitals and a symmetric peak shape.<sup>55</sup> In comparison with Figure S6, it can be deduced that two doublets (the Sb  $3d_{5/2}$  peaks at 529.5 and 528.5 eV and the respective Sb  $3d_{3/2}$  peaks at 538.9 and 537.9 eV) come from NAS. Using Figure S5, the Sb  $3d_{5/2}$  peak at 526.4 eV and the Sb  $3d_{3/2}$  peak at 535.8 eV can be attributed to  $\text{Na}_3\text{Sb}$ . This is reasonable as a less positive oxidation state corresponds to a shift toward lower binding energy.<sup>56</sup> The sodium oxide signal likely comes from species such as  $\text{Na}_2\text{SO}_3$  and  $\text{Na}_2\text{S}_2\text{O}_3$ , common impurities found in  $\text{Na}_2\text{S}$ . Ultimately, from the deconvolutions of the O 1s/Sb 3d region and S 2p region scans of the SSEI, both  $\text{Na}_3\text{Sb}$  and  $\text{Na}_2\text{S}$  are confirmed to form at the Na/NAS interface. These findings are in excellent agreement with our computational results. The low band gap of  $\text{Na}_3\text{Sb}$  clearly indicates an electronically conductive component of the SSEI, which facilitates the continuous formation and growth of the SSEI until proceeding to completion, resulting in the increase of the overall cell impedance over time. In turn, this results in the continuous increase in polarization with cycling, negatively impacting the battery performance and cycle life until cell failure.

The previous results suggest that bare NAS coupled with Na is unsuitable for a long-term ASSB due to the chemical instability which contributes to cell failure. We believe that modification of existing electrolytes or finding a suitable anode to improve the compatibility with Na metal are strategies to prolong the cycle life of ASSBs. One such modification applied in our previous work is Cl-doping of NPS, which was found to increase the room temperature ionic conductivity to over  $1 \text{ mS cm}^{-1}$ .<sup>25</sup> To investigate the effect of Cl-doping on the Na/NPS interfacial stability, symmetric cells using Na metal were assembled. A galvanic square-wave was pulsed through symmetric cells with NPS and NPSC, and the voltage was measured. The data is shown in Figure 8. To quantify the effect of the Cl-doping on the interface stability, the area-specific resistance (ASR) was then calculated following Ohm's law and using the area of the pellet,  $1.317 \text{ cm}^2$ . For the NPS, NPSC (6.25%), and NPSC (12.5%) samples, the calculated ASR grew from 1986 to 3740  $\Omega \text{ cm}^2$ , 992 to 2139  $\Omega \text{ cm}^2$ , and 6372 to 7163  $\Omega \text{ cm}^2$ , respectively, corresponding to percent increases of 88.3, 115.6, and 12.4%. A comparison of the ASR values is also shown in Figure 8d. Although the ASR of the 12.5% NPSC was

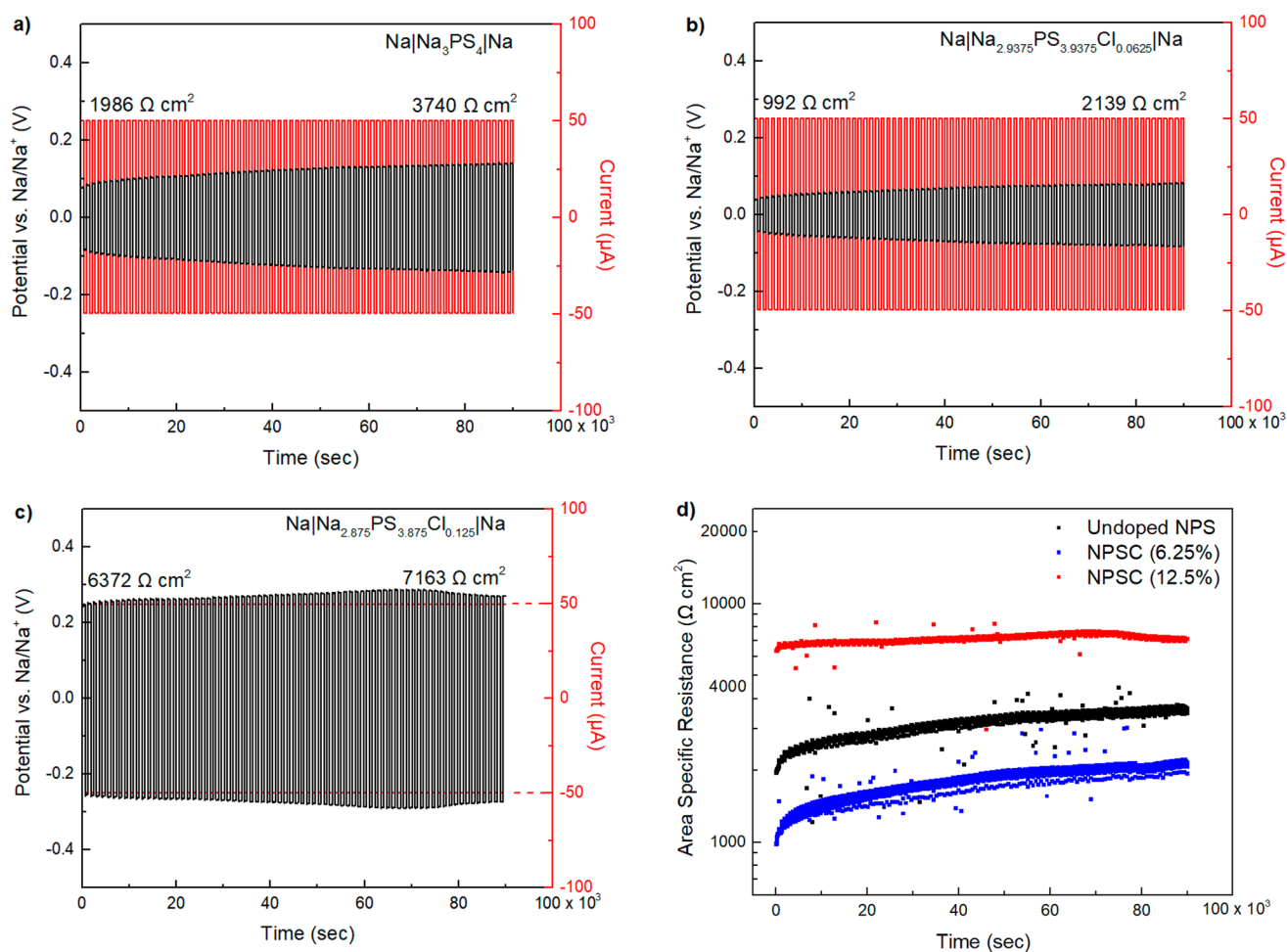


**Figure 8.** Galvanic square-wave cycling of (a) Na|NPS|Na symmetric cell and (b) Na|NPSC|Na ( $x = 6.25\%$ ) symmetric cell and (c) Na|NPSC|Na ( $x = 12.5\%$ ) symmetric cell. The ASR was calculated following Ohm's law. (d) Comparison of ASR versus time for the aforementioned symmetric cells.

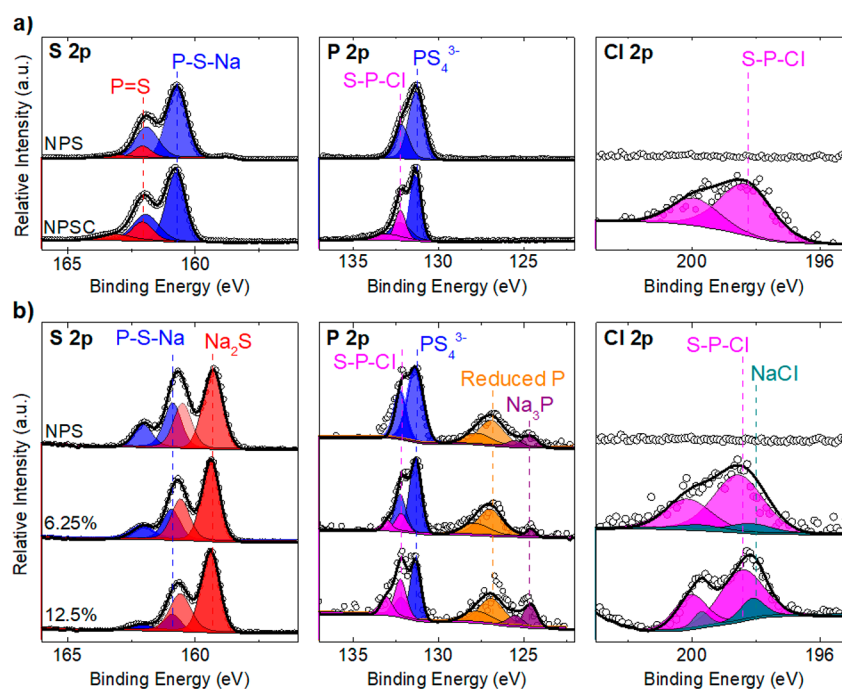
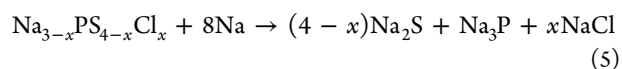
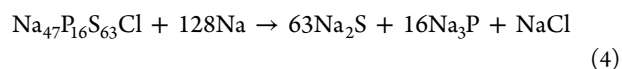


**Figure 9.** S 2p, P 2p, and Cl 2p region scans of (a) pristine NPS and NPSC and (b) SSEI after cycling of NPS, 6.25% doped NPSC, and 12.5% doped NPSC.

more stable over time, it had a much larger initial ASR. This suggests that there is an optimal Cl-doping concentration at which the highest conductivity for NPSC is achieved. These ASR values suggest that while further increasing the Cl content can improve interfacial stability, it will also lead to diminished conductivities by destabilizing the framework which could inhibit ionically conducting percolation pathways. This is supported by our previous computational results as increasing the concentration of Cl-doping from 6.25 to 12.5% increased the dopant formation energy from 0.96 to 1.77 eV.<sup>25</sup> This suggests that increased Cl-doping, which increases the concentration of Na vacancies, introduced more disorder in the structure. Taking the product of the ASR and the current density, the expected voltaic loss across the NPS interphase starts at approximately 100 mV and increases to almost 200 mV. In the 6.25% NPSC case, the overpotential increases from just under 50 mV to about 100 mV. The 12.5% NPSC cell had a voltaic loss of about 300 mV, most detrimental to the cyclability of the cell. This indicates that while increasing the Cl<sup>-</sup> content in the electrolyte can improve the stability of the interphase, there appears to be a compromise between stability and conductivity. The NPSC 6.25% cell, with the overall lower ASR, strikes the better balance between the two properties.

Full cells comprising of NPS and 6.25% NPSC were constructed, and the charge–discharge profile of the NPS and NPSC full-cells are shown in Figures S8a and S8b, respectively. The capacity and Coulombic efficiency are plotted in Figure S8c. After 10 cycles, the specific capacities of the NPS and NPSC cells were ~70 and 110 mAh g<sup>-1</sup>, respectively. Both cells show capacity fade, but it is important to note that the NPSC cell exhibited better capacity retention than the undoped NPS cell. Also, compared to our previous work, where the NPSC cell had a specific capacity of 80 mAh g<sup>-1</sup> after 10 cycles, the observed 110 mAh g<sup>-1</sup> for this NPSC cell is owed to better preparation and mixing of the composite cathode.<sup>25</sup> Ultimately, the better capacity retention suggests that Cl-doping improved the interfacial stability in a full cell; thus, doping the electrolyte could also be a promising strategy to improve the stability of NAS.

To investigate the products at the SSEI for the NPS and NPSC samples, the XPS spectra are shown in Figure 9. In NPS, we observe two spin–orbit doublets in the S 2p envelope that are characteristic of the P–S–Na (160.7 eV) and P=S (161.8 eV) bonding states. In the P 2p region, there is a single doublet associated with the tetrahedrally coordinated P in [PS<sub>4</sub>]<sup>3-</sup> at 131.3 eV. Upon cycling, there is the onset of a new spin–orbital doublet in the S 2p region; as with NAS, this peak is observed around 159.4 eV and attributed to Na<sub>2</sub>S.<sup>54</sup> In addition, two more spin–orbital doublets appear in the P 2p region after cycling; Na<sub>3</sub>P is found at 124.8 eV, and a reduced phosphorus phase is at 126.8 eV. These findings are consistent with those reported in previous literature.<sup>34</sup> For the doped samples (NPSC), the pristine spectrum is similar to NPS with an additional doublet in the P 2p and Cl 2p regions, ascribed to S–P–Cl bonding, indicating that Cl<sup>-</sup> was successfully incorporated in the [PS<sub>4</sub>]<sup>3-</sup> tetrahedra. After cycling, NaCl, a predicted decomposition product, is found at 198 eV.<sup>34</sup> All other decomposition products are similar to those of NPS. We speculate that the decomposition reaction is as follows for NPS and NPSC samples:



In this case, Na<sub>47</sub>P<sub>16</sub>S<sub>63</sub>Cl in eq 4 is an analogous stoichiometric ratio to 6.25% (atomic percent) Cl-doped Na<sub>3</sub>PS<sub>4</sub>. In the final equation, we demonstrate how the electrolyte could be synthetically designed to yield an interphase with a tunable salt content.

We find that NAS, NPS, and NPSC all degrade in the presence of Na metal, and this reaction proceeds gradually until completion to the detriment of electrochemical cell performance. In all three cases, this behavior is characteristic of the formation of an interphase with both ionic and electronic-conducting species. This is reasonable because although we find Na<sub>2</sub>S and polysulfides in the interphase, we also find Na<sub>3</sub>P for NPS and Na<sub>3</sub>Sb for NAS, which are known to have a low bandgap (0.4 and 0.68 eV, respectively). For NPSC, we also detect NaCl as a component in the interphase, which is an electronic insulator. NaCl could provide passivating qualities to improve cell performance, or in other words, slow the kinetics of the degradation. Moreover, in contrast to many other attempts to dope Na<sub>3</sub>PS<sub>4</sub> via a metallic cation (M<sup>4+</sup>, M = Si, Ge, Sn), NaCl advantageously suppresses electronic percolation through the SSE and the interphase.<sup>34</sup> Finally, we implemented the NPSC in an all-solid-state battery. The cell assembled with Na<sub>2.9375</sub>PS<sub>3.9375</sub>Cl<sub>0.0625</sub> retained more capacity with lower overpotentials over 10 cycles. We demonstrate that considering SSE compatibility with metallic anodes is essential to extend the lifetime of an ASSB.

## CONCLUSION

The decomposition mechanism for the solid electrolytes Na<sub>3</sub>SbS<sub>4</sub> and Na<sub>3</sub>PS<sub>4</sub> was investigated as these materials have good ionic conductivity but also are known to be unstable against Na metal, the latter being a persistent obstacle to wide-scale adoption of ASSBs. It was found that for these SSEs, the SSEI at the anode continuously grows into a thick layer, impeding electrochemical performance. In this work, XPS was applied to identify and confirm the compounds at the SSEI that were predicted computationally, which can provide insight on the cycling behavior of the battery. This methodology is a step toward more effective computational screening of SSE materials, as a favorable ionic conductivity of the electrolyte on its own is not sufficient to enable reversible all-solid-state batteries. The stability of a solid electrolyte against anodes and cathodes must be considered and evaluated to realize the most promising and practical solid-state battery chemistries. It was shown that electrolyte modification by Cl-doping of NPS is a method to improve cyclability as Cl-doping resulted in cells with better capacity retention compared to undoped NPS, suggesting Cl-doping can passivate or stabilize the interface. Future work such as evaluating other electrolytes in this manner, designing and optimizing the interfaces via electrolyte modification such as doping and mixing, analyzing different compounds for a suitable anode, or interface engineering with protective coatings for the metal anode or electrolyte all present worthwhile opportunities to gain a more complete understanding to improve the performance and longevity of Na ASSBs. In conjunction with these experimental evaluations, thermodynamic calculations and first-principles computation can help inform and accelerate such studies. Ultimately, the

goals of extending the cycle life and increasing the energy density through the use of metallic anodes remain paramount if ASSBs are to be viable.

## ■ ASSOCIATED CONTENT

### Supporting Information

The Supporting Information is available free of charge on the ACS Publications website at DOI: 10.1021/acsami.7b19037.

CVs, XRD patterns and data, DOS calculations, XPS binding energies and fit parameters, and galvanostatic cycling data (PDF)

## ■ AUTHOR INFORMATION

### Corresponding Authors

\*E-mail: a7banerjee@eng.ucsd.edu or abhikchm@gmail.com; Tel: +01-619-471-4716.

\*E-mail: shmeng@ucsd.edu; Tel: +01-858-822-4247; Fax: +01-858-534-9553.

### ORCID

Shyue Ping Ong: 0000-0001-5726-2587

Ying Shirley Meng: 0000-0001-8936-8845

### Notes

The authors declare no competing financial interest.

## ■ ACKNOWLEDGMENTS

The authors acknowledge the funding support from the National Science Foundation's Designing Materials to Revolutionize and Engineer our Future (DMREF) program under Grant 1436976. XPS was performed at the University of California, Irvine Materials Research Institute (IMRI) using instrumentation funded in part by the National Science Foundation Major Research Instrumentation Program under Grant CHE-1338173. We thank Ms. Hyeseung Chung for helping to collect the XPS data at UC Irvine and Dr. Curtis Moore and Dr. Milan Gembicky at the Crystallography Facility at the University of California, San Diego for assisting on the capillary XRD data collection. The characterization work was performed in part at the San Diego Nanotechnology Infrastructure (SDNI), a member of the National Nanotechnology Coordinated Infrastructure, which is supported by the National Science Foundation under Grant ECCS-1542148. The computations were performed using the Extreme Science and Engineering Discovery Environment (XSEDE), which is supported by National Science Foundation Grant ACI-1053575.

## ■ REFERENCES

- (1) Xu, K. Nonaqueous Liquid Electrolytes for Lithium-Based Rechargeable Batteries. *Chem. Rev.* **2004**, *104*, 4303–4417.
- (2) Goodenough, J. B.; Kim, Y. Challenges for Rechargeable Li Batteries. *Chem. Mater.* **2010**, *22* (3), 587–603.
- (3) Baggetto, L.; Niessen, R. A. H.; Roozeboom, F.; Notten, P. H. L. High Energy Density All-Solid-State Batteries: A Challenging Concept Towards 3D Integration. *Adv. Funct. Mater.* **2008**, *18*, 1057–1066.
- (4) Kamaya, N.; Homma, K.; Yamakawa, Y.; Hirayama, M.; Kanno, R.; Yonemura, M.; Kamiyama, T.; Kato, Y.; Hama, S.; Kawamoto, K.; Mitsui, A. A lithium superionic conductor. *Nat. Mater.* **2011**, *10*, 682–686.
- (5) Wang, L. P.; Yu, L.; Wang, X.; Srinivasan, M.; Xu, Z. Recent developments in electrode materials for sodium-ion batteries. *J. Mater. Chem. A* **2015**, *3*, 9353–9378.

(6) Wang, Y.; Richards, W. D.; Ong, S. P.; Miara, L. J.; Kim, J. C.; Mo, Y.; Ceder, G. Design principles for solid-state lithium superionic conductors. *Nat. Mater.* **2015**, *14*, 1026–1031.

(7) Bachman, J. C.; Muy, S.; Grimaud, A.; Chang, H.-H.; Pour, N.; Lux, S.; Paschos, O.; Maglia, F.; Lupart, S.; Lamp, P.; Giordano, L.; Shao-Horn, Y. Inorganic Solid-State Electrolytes for Lithium Batteries: Mechanisms and Properties Governing Ion Conduction. *Chem. Rev.* **2016**, *116* (1), 140–162.

(8) Massé, R.; Uchaker, E.; Cao, G. Beyond Li-ion: electrode materials for sodium- and magnesium-ion batteries. *Sci. China Mater.* **2015**, *58*, 715–766.

(9) Ellis, B.; Nazar, L. Sodium and sodium-ion energy storage batteries. *Curr. Opin. Solid State Mater. Sci.* **2012**, *16*, 168–177.

(10) Richards, W.; Tsujimura, T.; Miara, L.; Wang, Y.; Kim, J. C.; Ong, S. P.; Uechi, I.; Suzuki, N.; Ceder, G. Design and synthesis of the superionic conductor Na<sub>10</sub>SnP<sub>2</sub>S<sub>12</sub>. *Nat. Commun.* **2016**, *7*, 11009.

(11) Kundu, D.; Talaie, E.; Duffort, D.; Nazar, L. The Emerging Chemistry of Sodium Ion Batteries for Electrochemical Energy Storage. *Angew. Chem., Int. Ed.* **2015**, *54*, 3431–3448.

(12) Yabuuchi, N.; Kubota, K.; Dahbi, M.; Komaba, S. Research Development on Sodium-Ion Batteries. *Chem. Rev.* **2014**, *114* (23), 11636–11682.

(13) Song, S.; Duong, H. M.; Korsunsky, A. M.; Hu, N.; Lu, L. A Na<sup>+</sup> Superionic Conductor for Room-Temperature Sodium Batteries. *Sci. Rep.* **2016**, *6*, 32330.

(14) Deng, Z.; Mo, Y.; Ong, S. P. Computational studies of solid-state alkali conduction in rechargeable alkali-ion batteries. *NPG Asia Mater.* **2016**, *8*, e254.

(15) Tatsumisago, M.; Hayashi, A. Sulfide Glass-Ceramic Electrolytes for All-Solid-State Lithium and Sodium Batteries. *Int. J. Appl. Glas. Sci.* **2014**, *5*, 226–235.

(16) Pan, H.; Hu, Y.-S.; Chen, L. Room-temperature stationary sodium-ion batteries for large-scale electric energy storage. *Energy Environ. Sci.* **2013**, *6*, 2338.

(17) Hooper, A. A study of the electrical properties of single-crystal and polycrystalline  $\beta$ -alumina using complex plane analysis. *J. Phys. D: Appl. Phys.* **1977**, *10*, 1487–1496.

(18) Anantharamulu, N.; Rao, K.; Rambabu, G.; Kumar, B. V.; Radha, V.; Vithal, M. A wide-ranging review on Nasicon type materials. *J. Mater. Sci.* **2011**, *46*, 2821–2837.

(19) Bo, S.-H.; Wang, Y.; Kim, J. C.; Richards, W. D.; Ceder, G. Computational and Experimental Investigations of Na-Ion Conduction in Cubic Na<sub>3</sub>PSe<sub>4</sub>. *Chem. Mater.* **2016**, *28*, 252–258.

(20) Chu, I.-H.; Nguyen, H.; Hy, S.; Lin, Y.-C.; Wang, Z.; Xu, Z.; Deng, Z.; Meng, Y. S.; Ong, S. P. Insights into the Performance Limits of the Li<sub>7</sub>P<sub>3</sub>S<sub>11</sub> Superionic Conductor: A Combined First-Principles and Experimental Study. *ACS Appl. Mater. Interfaces* **2016**, *8*, 7843–7853.

(21) Zhang, L.; Yang, K.; Mi, J.; Lu, L.; Zhao, L.; Wang, L.; Li, Y.; Zeng, H. Na<sub>3</sub>PSe<sub>4</sub>: A Novel Chalcogenide Solid Electrolyte with High Ionic Conductivity. *Adv. Energy Mater.* **2015**, *5*, 1501294.

(22) Sakuda, A.; Hayashi, A.; Tatsumisago, M. Sulfide Solid Electrolyte with Favorable Mechanical Property for All-Solid-State Lithium Battery. *Sci. Rep.* **2013**, *3*, 2261.

(23) Zhang, L.; Zhang, D.; Yang, K.; Yan, X.; Wang, L.; Mi, J.; Xu, B.; Li, Y. Vacancy-Contained Tetragonal Na<sub>3</sub>SbS<sub>4</sub> Superionic Conductor. *Adv. Sci.* **2016**, *3*, 1600089.

(24) Banerjee, A.; Park, K. H.; Heo, J. W.; Nam, Y. J.; Moon, C. K.; Oh, S. M.; Hong, S.-T.; Jung, Y. S. Na<sub>3</sub>SbS<sub>4</sub>: A Solution Processable Sodium Superionic Conductor for All-Solid-State Sodium-Ion Batteries. *Angew. Chem., Int. Ed.* **2016**, *55*, 1–6.

(25) Chu, I.-H.; Kompella, C.; Nguyen, H.; Zhu, Z.; Hy, S.; Deng, Z.; Meng, Y. S.; Ong, S. P. Room-Temperature All-solid-state Rechargeable Sodium-ion Batteries with a Cl-doped Na<sub>3</sub>PS<sub>4</sub> Superionic Conductor. *Sci. Rep.* **2016**, *6*, 33733.

(26) Yu, C.; Ganapathy, S.; de Klerk, N.; van Eck, E.; Wagemaker, M. Na-ion dynamics in tetragonal and cubic Na<sub>3</sub>PS<sub>4</sub> a Na-ion conductor for solid state Na-ion batteries. *J. Mater. Chem. A* **2016**, *4*, 15095–15105.

- (27) Hayashi, A.; Noi, K.; Tanibata, N.; Nagao, M.; Tatsumisago, M. High sodium ion conductivity of glass–ceramic electrolytes with cubic  $\text{Na}_3\text{PS}_4$ . *J. Power Sources* **2014**, *258*, 420–423.
- (28) Nguyen, H.; Hy, S.; Wu, E.; Deng, Z.; Samiee, M.; Yersak, T.; Luo, J.; Ong, S. P.; Meng, Y. S. Experimental and Computational Evaluation of a Sodium-Rich Anti-Perovskite for Solid State Electrolytes. *J. Electrochem. Soc.* **2016**, *163* (10), A2165–A2171.
- (29) Wang, Y.; Wang, Q.; Liu, Z.; Zhou, Z.; Li, S.; Zhu, J.; Zou, R.; Wang, Y.; Lin, J.; Zhao, Y. Structural manipulation approaches towards enhanced sodium ionic conductivity in Na-rich antiperovskites. *J. Power Sources* **2015**, *293*, 735–740.
- (30) Jansen, M.; Henseler, U. Synthesis, structure determination, and ionic conductivity of sodium tetrathiosphosphate. *J. Solid State Chem.* **1992**, *99* (1), 110–119.
- (31) Hayashi, A.; Noi, K.; Sakuda, A.; Tatsumisago, M. Superionic glass-ceramic electrolytes for room-temperature rechargeable sodium batteries. *Nat. Commun.* **2012**, *3*, 856.
- (32) Hibi, Y.; Tanibata, N.; Hayashi, A.; Tatsumisago, M. Preparation of sodium ion conducting  $\text{Na}_3\text{PS}_4$ – $\text{NaI}$  glasses by a mechanochemical technique. *Solid State Ionics* **2015**, *270*, 6–9.
- (33) Tanibata, N.; Noi, K.; Hayashi, A.; Tatsumisago, M. Preparation and characterization of highly sodium ion conducting  $\text{Na}_3\text{PS}_4$ – $\text{Na}_4\text{SiS}_4$  solid electrolytes. *RSC Adv.* **2014**, *4*, 17120.
- (34) Wenzel, S.; Leichtweiss, T.; Weber, D. A.; Sann, J.; Zeier, W. G.; Janek, J. Interfacial Reactivity Benchmarking of the Sodium Ion Conductors  $\text{Na}_3\text{PS}_4$  and Sodium  $\beta$ -Alumina for Protected Sodium Metal Anodes and Sodium All-Solid-State Batteries. *ACS Appl. Mater. Interfaces* **2016**, *8*, 28216–28224.
- (35) Rodriguez-Carvajal, J.; Rousse, G.; Masquelier, C.; Hervieu, M. Electronic Crystallization in a Lithium Battery Material: Columnar Ordering of Electrons and Holes in the Spinel  $\text{LiMn}_2\text{O}_4$ . *Phys. Rev. Lett.* **1998**, *81*, 4660–4663.
- (36) Brug, G. J.; van den Eeden, A. L. G.; Sluyters-Rehbach, M.; Sluyters, J. H. The Analysis of Electrode Impedances Complicated by the Presence of a Constant Phase Element. *J. Electroanal. Chem. Interfacial Electrochem.* **1984**, *176*, 275–295.
- (37) Heyd, J.; Scuseria, G. E. Efficient hybrid density functional calculations in solids: Assessment of the Heyd–Scuseria–Ernzerhof screened Coulomb hybrid functional. *J. Chem. Phys.* **2004**, *121*, 1187.
- (38) Heyd, J.; Scuseria, G. E.; Ernzerhof, M. Hybrid functionals based on a screened Coulomb potential. *J. Chem. Phys.* **2003**, *118*, 8207.
- (39) Heyd, J.; Scuseria, G. E.; Ernzerhof, M. Erratum: “Hybrid functionals based on a screened Coulomb potential” [*J. Chem. Phys.* **118**, 8207 (2003)]. *J. Chem. Phys.* **2006**, *124*, 219906.
- (40) Whittingham, M. S. Chemistry of Intercalation Compounds: Metal Guests in Chalcogenide Hosts. *Prog. Solid State Chem.* **1978**, *12*, 41–99.
- (41) Conroy, L.; Park, K. C. Electrical properties of the Group IV disulfides, titanium disulfide, zirconium disulfide, hafnium disulfide and tin disulfide. *Inorg. Chem.* **1968**, *7* (3), 459–463.
- (42) Zhang, D.; Cao, X.; Xu, D.; Wang, N.; Yu, C.; Hu, W.; Yan, X.; Mi, J.; Wen, B.; Wang, L.; Zhang, L. Synthesis of cubic  $\text{Na}_3\text{SbS}_4$  solid electrolyte with enhanced ion transport for all-solid-state sodium-ion batteries. *Electrochim. Acta* **2018**, *259*, 100–109.
- (43) Han, F.; Zhu, Y.; He, X.; Mo, Y.; Wang, C. Electrochemical Stability of  $\text{Li}_{10}\text{GeP}_2\text{S}_{12}$  and  $\text{Li}_7\text{La}_3\text{Zr}_2\text{O}_{12}$  Solid Electrolytes. *Adv. Energy Mater.* **2016**, *6*, 1501590.
- (44) Yue, J.; Han, F.; Fan, X.; Zhu, X.; Ma, Z.; Yang, J.; Wang, C. High-Performance All-Inorganic Solid-State Sodium-Sulfur Battery. *ACS Nano* **2017**, *11*, 4885–4891.
- (45) Zhang, W.; Leichtweiß, T.; Culver, S.; Koerver, R.; Das, D.; Weber, D.; Zeier, W.; Janek, J. The Detrimental Effects of Carbon Additives in  $\text{Li}_{10}\text{GeP}_2\text{S}_{12}$ -Based Solid-State Batteries. *ACS Appl. Mater. Interfaces* **2017**, *9*, 35888–35896.
- (46) Hakari, T.; Sato, Y.; Yoshimi, S.; Hayashi, A.; Tatsumisago, M. Favorable Carbon Conductive Additives in  $\text{Li}_3\text{PS}_4$  Composite Positive Electrode Prepared by Ball-Milling for All-Solid-State Lithium Batteries. *J. Electrochem. Soc.* **2017**, *164* (12), A2804–A2811.
- (47) Chen, C. H.; Liu, J. H.; Amine, K. Symmetric cell approach and impedance spectroscopy of high power lithium-ion batteries. *J. Power Sources* **2001**, *96*, 321–328.
- (48) Nara, H.; Morita, K.; Yokoshima, T.; Mukoyama, D.; Momma, T.; Osaka, T. Electrochemical impedance spectroscopy analysis with a symmetric cell for  $\text{LiCoO}_2$  cathode degradation correlated with Co dissolution. *AIMS Materials Science* **2016**, *3* (2), 448–459.
- (49) Zhang, X.; Zhang, W.; Lei, G. A Review of Li-ion Battery Equivalent Circuit Models. *Transactions of Electrical and Electronic Materials* **2016**, *17* (6), 311–316.
- (50) Chang, M.-T.; Lin, Y.-S.; Ling, S. H.; Liang, S. H.; Lin, C. H.; Chen, K. C. Identification of the Parameters in Equivalent Circuit Model of Lithium-Ion Batteries. *ECS Trans.* **2014**, *61* (27), 125–130.
- (51) Bron, P.; Roling, B.; Dehnen, S. Impedance characterization reveals mixed conducting interphases between sulfidic superionic conductors and lithium metal electrodes. *J. Power Sources* **2017**, *352*, 127–134.
- (52) Ettema, A. R. H. F.; de Groot, R. A. Electronic structure of  $\text{Na}_3\text{Sb}$  and  $\text{Na}_2\text{KSb}$ . *Phys. Rev. B: Condens. Matter Mater. Phys.* **2000**, *61* (15), 10035.
- (53) Bertheville, B.; Low, D.; Kubel, F.; Bill, H. Ionic conductivity of  $\text{Na}_2\text{S}$  single crystals between 295 and 1350 K experimental setup and first results. *J. Phys. Chem. Solids* **1997**, *58* (10), 1569–1577.
- (54) Tanibata, N.; Deguchi, M.; Hayashi, A.; Tatsumisago, M. All-Solid-State Na/S Batteries with a  $\text{Na}_3\text{PS}_4$  Electrolyte Operating at Room Temperature. *Chem. Mater.* **2017**, *29*, 5232–5238.
- (55) Qi, Z.; Lan, H.; Joshi, T.; Liu, R.; Liu, H.; Qu, J. Enhanced oxidative and adsorptive capability towards antimony by copper-doping into magnetite magnetic particles. *RSC Adv.* **2016**, *6*, 66990.
- (56) Dobler, D.; Oswald, S.; Wetzig, K. Calibration of XPS – energy scale for determination of the oxidation states of doping elements in  $\text{SnO}_2$  powders. *Anal. Bioanal. Chem.* **2002**, *374*, 646.